Optics Letters

Designing optical fields in inhomogeneous media

YOUSUF ABORAHAMA AND MO MOJAHEDI*

The Edward S. Rogers Department of Electrical and Computer Engineering, University of Toronto, 10 King's College Road, Toronto, Ontario M5S 3G4, Canada
**Corresponding author: mojahedi@waves.utoronto.ca*

Received 18 August 2021; revised 17 September 2021; accepted 17 September 2021; posted 17 September 2021 (Doc. ID 438534); published 15 October 2021

Designing optical fields with predetermined properties in source-free inhomogeneous media has been a long-sought goal due to its potential utilization in many applications, such as optical trapping, micromachining, imaging, and data communications. Using ideas from the calculus of variations, we provide a general framework based on the Helmholtz equation to design optical fields with prechosen amplitude and phase inside an inhomogeneous medium. The generated field is guaranteed to be the closest physically possible rendition of the desired field. The developed analytical approach is then verified via different techniques, where the approach's validity is demonstrated by generating the desired optical fields in different inhomogeneous media. © 2021 Optical Society of America

https://doi.org/10.1364/OL.438534

Manipulating the intensity and phase of optical fields inside source-free media has been an important goal that many researchers have strived to achieve. Such ability is useful for various applications such as optical micromanipulations [1,2], data communications [3,4], imaging [5,6], ultracold atoms [7,8], and remote sensing [9,10], to name a few. However, any optical field must obey Maxwell's equations to be physically realizable. In other words, not any arbitrarily chosen amplitude and phase associated with an optical field is physically permitted. Nevertheless, recent advances in the design of spatial light modulators (SLMs), metasurfaces, and Q-plates have given researchers some additional tools to elude the aforementioned constraints to one degree or another.

Many researchers have attempted to achieve the aforementioned goal by generating new classes of beams that exhibit some unusual properties. Self-accelerating beams, such as Airy beams [11], are examples of such attempts. In addition to following curved trajectories, these beams can resist diffraction and share the self-healing property with many other non-diffracting beams [12,13]. Frozen waves are another example of non-diffracting beams, which consist of superpositions of co-propagating Bessel beams to generate beams with exotic axial intensity profiles and/or the ability to change the beam's orbital angular momentum (OAM) and polarization locally [14–16]. While all the above-mentioned techniques are subject to the paraxial approximation, researchers have been able to generate several classes of nonparaxial accelerating beams (NABs) such as circular NABs [17] and Mathieu and Weber accelerating beams [18]. Numerical and iterative techniques are alternative approaches that have been sought by some researchers [19–22]. One of the most iconic iterative techniques, based on the Gerchberg–Saxton (GS) algorithm, has been used to generate different intensity patterns via iteratively adjusting the phase of the optical field at the SLM plane [21]. Needless to say, these techniques tend to be computationally expensive and do not reveal the system's underlying physics. More importantly, to the best of our knowledge, no numerical or iterative technique has been used to arbitrarily design the phase and amplitude of light inside an inhomogeneous medium.

In this Letter, we provide a general framework that can be used to generate any desired optical field inside a source-free inhomogeneous medium, without the need to alter the medium's index of refraction. The generated optical field is guaranteed to be the closest possible rendition of the desired field, which is also a solution to the Helmholtz equation. The provided framework is verified via simulations by generating two optical fields in different inhomogeneous media that are either slowly varying or include scattering objects such as dielectric walls.

To obtain the previously described solution, let $\Omega \subset \mathbb{R}^m$ be a bounded open region with a piecewise smooth boundary $\partial\Omega$ in a source-free inhomogeneous medium, and let $\Phi : \bar{\Omega} \to \mathbb{C}$ be any desired complex-valued scalar field that does not necessarily satisfy the Helmholtz equation inside Ω (here, $\bar{\Omega}$ refers to the closure of Ω). We seek a solution to the Helmholtz equation that is the closest possible rendition of our desired field, Φ, in the same region. To be precise, we seek $\Psi : \bar{\Omega} \to \mathbb{C}$ that minimizes

$$\mathcal{E} = \int_\Omega \frac{1}{2}|\Psi(\boldsymbol{x}) - \Phi(\boldsymbol{x})|^2 \mathrm{d}^m\boldsymbol{x}, \tag{1}$$

subject to the constraint

$$\nabla^2\Psi(\boldsymbol{x}) + k^2(\boldsymbol{x})\Psi(\boldsymbol{x}) = 0, \quad \forall \boldsymbol{x} \in \Omega, \tag{2}$$

where both $\Psi(\boldsymbol{x})$ and $\Phi(\boldsymbol{x})$ are assumed to be bounded and sufficiently smooth on Ω, and $k(\boldsymbol{x}) = \omega n(\boldsymbol{x})/c$ is the wavenumber, which can be complex in the case of lossy or gain media.

To account for the constraint imposed by Eq. (2), we define a sufficiently smooth complex-valued adjoint function, $\Lambda : \bar{\Omega} \to \mathbb{C}$. Hence, the resulting functional $\mathcal{J}$ will be

$$F = \mathcal{J}[\Psi] = \int_\Omega \frac{1}{2}|\Psi(\boldsymbol{x}) - \Phi(\boldsymbol{x})|^2 + \mathrm{Re}\left(\Lambda^*(\boldsymbol{x})(\nabla^2\Psi(\boldsymbol{x}) + k^2(\boldsymbol{x})\Psi(\boldsymbol{x}))\right) \mathrm{d}^m\boldsymbol{x}, \quad (3)$$

where F denotes the value assigned by $\mathcal{J}$ for a given function Ψ, Re$(\cdot)$ stands for the real part, and Λ^* is the complex conjugate of Λ. Next, we introduce a complex variation $\delta\Psi = \delta\Psi_R + i\delta\Psi_I$ to Ψ in Eq. (3) and expand the integrand keeping only the first-order terms in the real and imaginary parts of $\delta\Psi$, which leads to the first-order variation of F with respect to Ψ. Using Green's second identity and after some mathematical manipulations [23], one can obtain the stationarity conditions

$$\nabla^2\Lambda(\boldsymbol{x}) + (k^*(\boldsymbol{x}))^2\Lambda(\boldsymbol{x}) + \Psi(\boldsymbol{x}) = \Phi(\boldsymbol{x}), \ \forall \boldsymbol{x} \in \Omega, \quad (4a)$$

$$\Lambda(\boldsymbol{x}) = 0, \ \nabla\Lambda(\boldsymbol{x}) \cdot N(\boldsymbol{x}) = 0, \quad \forall \boldsymbol{x} \in \partial\Omega, \quad (4b)$$

where $N(\boldsymbol{x})$ is the outward unit normal vector to the boundary $\partial\Omega$. Now, by isolating $\Psi(\boldsymbol{x})$ in Eq. (4a) and substituting it into the Helmholtz equation [Eq. (2)], we arrive at a single fourth-order partial differential equation (PDE) with homogeneous Cauchy boundary conditions (BCs)

$$\nabla^4\Lambda + k^2\nabla^2\Lambda + \nabla^2((k^*)^2\Lambda) + |k|^4\Lambda = \nabla^2\Phi + k^2\Phi, \quad \forall \boldsymbol{x} \in \Omega, \quad (5a)$$

$$\Lambda = 0, \ \nabla\Lambda \cdot N = 0, \quad \forall \boldsymbol{x} \in \partial\Omega, \quad (5b)$$

where $\nabla^4 \equiv \nabla^2\nabla^2$. For a given $\Phi(\boldsymbol{x})$, once the boundary value problem (BVP) in Eq. (5) is solved, the optical field $\Psi(\boldsymbol{x})$ can be computed from Eq. (4a) according to

$$\Psi(\boldsymbol{x}) = \Phi(\boldsymbol{x}) - (\nabla^2\Lambda(\boldsymbol{x}) + (k^*(\boldsymbol{x}))^2\Lambda(\boldsymbol{x})). \quad (6)$$

The values of the optical field obtained from Eq. (6) at the boundary can then be used to produce a hologram that will be projected onto an SLM (or a metasurface), consequently generating the desired field, or its closest possible realization (in the L^2-norm sense), in a given spatial domain Ω.

In the case of a smoothly varying index of refraction, Eq. (5a) can be rewritten as

$$\nabla^4\Lambda + 2\mathrm{Re}(k^2)\nabla^2\Lambda + 4k^*\nabla k^* \cdot \nabla\Lambda + (\nabla^2 k^* + |k|^4)\Lambda = \nabla^2\Phi + k^2\Phi, \quad \forall x \in \Omega. \quad (7)$$

It is worth comparing Eq. (7) to the special case in Ref. [19]. The appearance of "Re$(\cdot)$" in the second term and the modulus in the last term of the left-hand side are due to the fact that we are allowing k to be complex-valued to account for the loss or gain. As for the change due to the variation of the index of refraction, it appears in two additional terms ($\nabla^2 k^*\Lambda$ and $4k^*\nabla k^* \cdot \nabla\Lambda$). These two terms can be neglected in the case of a medium with a slowly varying index of refraction, and of course, in the case of a homogeneous medium, Eq. (7) will reduce to the simple cases discussed in Ref. [19].

After defining the pattern of interest ($\Phi(\boldsymbol{x})$), the wavelength, and the inhomogeneous medium (using k and Ω), the next step toward designing the optical field is to solve the BVP in Eq. (5). To do so, we have used the finite-difference method (FDM). The BVP in Eq. (5) is discretized using second-order finite differences resulting in a system of linear equations. This system is then solved using the LU-decomposition (for the 2D case) and the biconjugate gradient method (for the 3D case).

For the optical fields designed in this work, we choose the region Ω to be a square (in the case of 2D) or a cube (in the case of 3D). However, it is worth keeping in mind that although the field $\Psi(\boldsymbol{x})$—obtained from Eq. (5) and Eq. (6)—is guaranteed to satisfy the Helmholtz equation, in practice, when a beam is freely traveling in an unbounded medium, the experimenter often has access to only one boundary plane (i.e., the plane of the SLM or metasurface). Thus, to eliminate the contributions from the other boundaries, absorbing layers have been placed in front of all boundaries except the one associated with the SLM or metasurface.

Having used FDM to obtain the solutions to Eq. (5), we have verified the validity of our approach by designing two desired optical fields inside different inhomogeneous media. The behavior of these optical fields is then simulated using the finite-element method (FEM), and the finite-difference time-domain (FDTD) method as further verification, and to obtain the time-domain behavior. The FEM simulation was carried in COMSOL Multiphysics, while the FDTD simulation was performed using Lumerical. In the FEM simulation of the first example, instead of imposing the values of the electric field at the boundary as a BC, a surface current density (source) was used with a perfectly matched layer to absorb the backward traveling radiations from that source. This choice was made so that the simulations more closely resemble the physical experimental conditions. In other words, one may recall that in actual experimental setups, the excitation fields are generated by the sources, whereas the BCs are the superposition of both the field generated by the sources and the field scattered from the objects. Having said that, it is important to mention that although our proposed method provides us with the required BCs, in practice, one can still use the calculated BCs without the extra effort of evaluating the surface current densities when the scattered fields near the source are relatively small.

As the first example, we have designed a beam that while traveling in the air encounters two walls made of fused silica ($n = 1.46$). Each wall is 0.5 μm thick in the x-direction and 5 μm long in the y-direction (see Fig. 1). The walls are placed so that there is no line of sight when looking toward the x-direction. The study of such a case can be useful for many applications such as imaging and optical trapping beyond barriers. The goal here is to design a structured beam that, upon scattering from the walls, clears the obstacles and continues to travel along the original trajectory. Figure 1(a) shows the result of our FEM simulation, whereas the movie (Visualization 1) displays the dynamics of the beam evolution obtained using the FDTD simulation. For comparison, the behavior of a Gaussian beam, of approximately the same size and polarization, upon scattering from the same pair of walls, can be found in Fig. 1(b). From Fig. 1(b), it should be evident that the Gaussian beam, unlike the structured beam, is incapable of clearing out the obstacles. We have also plotted the magnitude of the electric field (blue) and its phase (red with markers) for the structured beam at the boundary plane ($x = 0$) in Fig. 1(c). Since the walls are placed at different distances from the source, the magnitude and the phase of the field at the boundary plane are asymmetric with respect to the y-axis.

As alluded to earlier, the dynamics of beam propagation and its interactions with the barriers (walls) can be better visualized

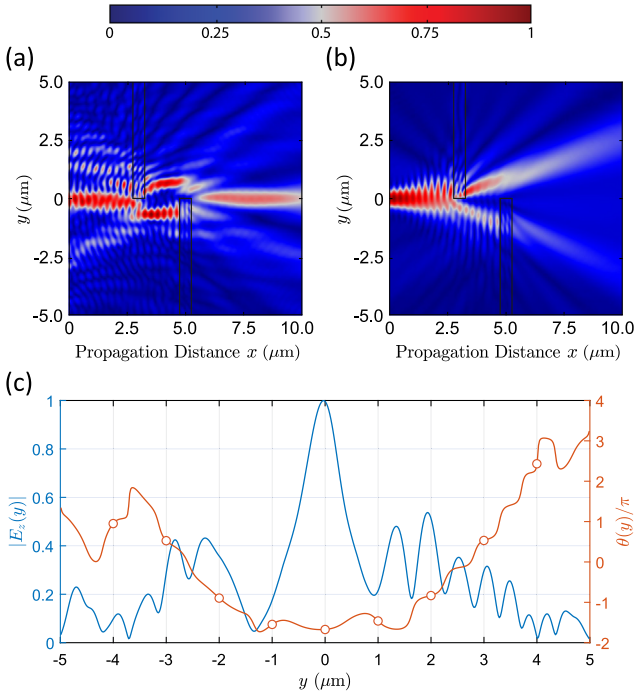

Fig. 1. Bypassing a pair of walls. (a) Magnitude of the electric field of the structured beam upon encountering a pair of walls ($n = 1.46$), which allows no line of sight along the x-direction. (b) Magnitude of the electric field of a Gaussian beam of approximately the same size as the structured beam, facing the same walls. (c) Normalized magnitude of the electric field (blue) and unwrapped phase (red with markers) of the structured beam at the $x = 0$ boundary.

and analyzed using the movie (Visualization 1). As the movie indicates, the structured beam, upon scattering from the first wall, splits into two main parts. This is similar to what happens to the Gaussian beam [see Fig. 1(b)], albeit upon scattering from the first wall, the angle that the structured beam makes with the horizontal axis (x-axis here) is much shallower than the angle that the Gaussian beam makes with the horizontal axis. In the case of the structured beam, one of the two aforementioned main parts (upper section) essentially avoids interactions with the second barrier, whereas the other part (lower section) scatters from the second barrier at almost normal incidence, where upon emerging from the second barrier, it constructively interferes with the upper section, hence producing an overall beam that continues on a straight path.

For our next example, we consider a medium with a continuously varying index of refraction given by $n = 1.4 + 8 \times 10^4 y$. Our goal here is to design a 3D beam that, despite the medium continuous inhomogeneity, follows a straight path inside the medium. This type of inhomogeneous media can be encountered both artificially in manufactured media such as graded-index materials and naturally in situations similar to the hot-road mirage, although, for our example, we have purposefully chosen a much stronger variation in the index of refraction to demonstrate the capabilities of the proposed approach. Figure 2(a) shows the intensity pattern of our designed beam (structured beam), whereas Fig. 2(b) displays the situation for a Gaussian beam of approximately the same size and polarization traveling in the same medium. From the figures, it should be clear that the structured beam follows the required straight path, whereas, on the other hand, the Gaussian beam bends upward

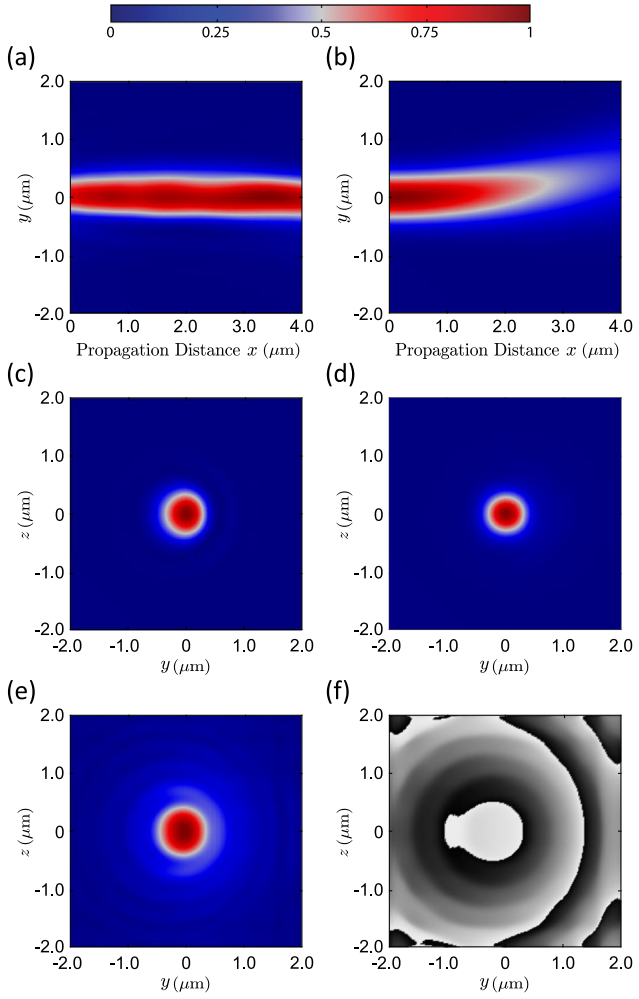

Fig. 2. Nonbending beam. (a) Intensity pattern for our designed beam traveling along a straight line in a medium with a continuously varying index of refraction ($n = 1.4 + 10^4 y$). (b) Intensity pattern of a Gaussian beam traveling in the same medium. (c) Intensity of the optical field at the $x = 2$ μm plane. (d) Intensity of the optical field at the $x = 4$ μm plane. (e) Modulus of the z component of the electric field at the $x = 0$ plane (i.e., boundary plane). (f) Phase of the z component of the electric field at the $x = 0$ plane, which varies from zero (black) to 2π (white).

as a consequence of the increased index of refraction in that direction. Figures 2(c) and 2(d) show the intensity of the field in the transverse planes $x = 2$ μm and $x = 4$ μm, respectively.

A closer examination of the intensities at the transverse planes shows that the rings around the beam's central spot are not concentric (unlike the Bessel beams propagating in vacuum, for example), but rather shifted to the left toward the lower index region, even though the beam's central spot continues to travel along a straight line. We have also plotted the modulus of the z-component of the normalized electric field ($|E_z(0, y, z)|$) and its phase at the $x = 0$ boundary plane in Figs. 2(e) and 2(f), respectively. The aforementioned field modulus and phase are in fact the BCs used to generate the optical field in this example. Last, the time-domain behavior of this structured beam can be found in Visualization 2. From the movie, it can be seen that as the beam propagates, the rings shift upward, while the center spot continues on a straight line.

At this point, it is important to discuss a few additional details regarding the proposed method and the results presented in this Letter. First, for the results presented here, the electric field is polarized along the z-direction. This polarization was chosen to ensure that the Helmholtz equation is the correct constraint on the field's behavior in the case of a 2D region. However, it is possible to consider other polarizations; in such cases, one must assume that the index of refraction is slowly varying to ensure that the Helmholtz equation still describes the dynamics of wave propagation in the medium with reasonable accuracy. In future analyses, this shortcoming can be addressed by considering Maxwell's equations as the constraint. Second, it is important to keep in mind that the goal of the current approach is to obtain an optical field $\Psi(\boldsymbol{x})$ that, while it satisfies the Helmholtz equation, is also the closest rendition of the desired field, $\Phi(\boldsymbol{x})$. This then presupposes that the user has some ideas of the desired field suitable for his/her application. We should also keep in mind that $\Phi(\boldsymbol{x})$ is a complex-valued scalar field; hence, one should specify both the intensity and phase of the pattern of interest. For instance, in the case of the examples presented here, we had chosen beams whose intensity pattern in the transverse plane displays a Gaussian profile, while their phase is a linear function of the index of refraction (for further information, see Supplement 1). Third, the counterintuitive behaviors of the optical beams, depicted in Figs. 1 and 2, are due to the interference phenomenon and do not violate any of the known conservation laws (e.g., energy and/or momentum). This can be further verified via more detailed calculations of the energy and momentum associated with the structured beams. Fourth, in Supplement 1, we have provided two additional examples of optical fields in different inhomogeneous media.

Finally, a short discussion of the future experimental realization of our theoretical results presented here is in order. The experimental setup that can be used to verify the behavior of our structured beams consists of an SLM, a 4f system, an iris, a CCD camera, and a few lenses used in a telescopic configuration, similar to the approach discussed in Ref. [24]. In such an approach, the desired BCs obtained from Eq. (6) will be transformed to a 2D hologram then projected onto an SLM. A Gaussian beam incident on the SLM will be modulated, and the iris along with the 4f system will be used to pick the needed diffraction order from the modulated Gaussian beam. This allows us to remove the on-axis carrier and select only the desired pattern encoded in a higher diffraction order. To account for the generation of the structured beams in micrometer scale, given the limitations imposed by the relatively larger pixel pitch of the SLM, the hologram can be digitally magnified before being displayed on the SLM, and a microscope objective lens can then be used in a telescopic configuration after the 4f system to shrink the beam's transverse profile. An imaging system consists of another lens, and a microscope objective lens can be used to image a magnified copy of the transverse beam's intensity profile using a CCD camera. This imaging system is usually mounted on a translation stage to record the transverse profile of the magnified beam at consecutive planes along the propagation direction, in a way such that the longitudinal profile of the beam can then be reconstructed. Note that one still needs to have the inhomogeneous medium of interest after the $x = 0$ plane in addition to being able to place the imaging system in the locations over which he/she is interested in imaging the optical field.

In conclusion, using ideas from the calculus of variations, we have developed a BVP, the solution of which can be used to generate exotic complex-valued scalar optical fields inside inhomogeneous media. We have further demonstrated the suitability of our approach by generating two optical fields inside two different inhomogeneous media. In the future, it would be interesting to extend the current approach to 3D vectorial optical fields subject to Maxwell's equations and investigate the control of such fields in predefined inhomogeneous and/or anisotropic media.

Funding. Natural Sciences and Engineering Research Council of Canada (RGPIN-2017-06052).

Disclosures. The authors declare no conflicts of interest.

Data Availability. Data underlying the results presented in this paper are not publicly available at this time but may be obtained from the authors upon reasonable request.

Supplemental document. See Supplement 1 for supporting content.

REFERENCES

1. Y. Li, L.-M. Zhou, and N. Zhao, Opt. Lett. **46**, 106 (2021).
2. J. A. Rodrigo, T. Alieva, E. Abramochkin, and I. Castro, Opt. Express **21**, 20544 (2013).
3. L. Gong, Q. Zhao, H. Zhang, X.-Y. Hu, K. Huang, J.-M. Yang, and Y.-M. Li, Light Sci. Appl. **8**, 27 (2019).
4. A. E. Willner, H. Huang, Y. Yan, Y. Ren, N. Ahmed, G. Xie, C. Bao, L. Li, Y. Cao, Z. Zhao, J. Wang, M. P. J. Lavery, M. Tur, S. Ramachandran, A. F. Molisch, N. Ashrafi, and S. Ashrafi, Adv. Opt. Photon. **7**, 66 (2015).
5. B. Yin, Z. Piao, K. Nishimiya, C. Hyun, J. A. Gardecki, A. Mauskapf, F. A. Jaffer, and G. J. Tearney, Light Sci. Appl. **8**, 104 (2019).
6. Y. Xue, K. P. Berry, J. R. Boivin, C. J. Rowlands, Y. Takiguchi, E. Nedivi, and P. T. So, Optica **6**, 76 (2019).
7. M. Andersen, C. Ryu, P. Cladé, V. Natarajan, A. Vaziri, K. Helmerson, and W. D. Phillips, Phys. Rev. Lett. **97**, 170406 (2006).
8. A. Ramanathan, K. Wright, S. Muniz, M. Zelan, W. Hill, III, C. Lobb, K. Helmerson, W. Phillips, and G. Campbell, Phys. Rev. Lett. **106**, 130401 (2011).
9. A. H. Dorrah, M. Zamboni-Rached, and M. Mojahedi, Light Sci. Appl. **7**, 40 (2018).
10. N. Cvijetic, G. Milione, E. Ip, and T. Wang, Sci. Rep. **5**, 15422 (2015).
11. G. Siviloglou, J. Broky, A. Dogariu, and D. N. Christodoulides, Phys. Rev. Lett. **99**, 213901 (2007).
12. J. Broky, G. A. Siviloglou, A. Dogariu, and D. N. Christodoulides, Opt. Express **16**, 12880 (2008).
13. H. E. Hernández-Figueroa, M. Zamboni-Rached, and E. Recami, *Non-Diffracting Waves* (Wiley, 2013).
14. A. H. Dorrah, M. Zamboni-Rached, and M. Mojahedi, Appl. Phys. Lett. **110**, 051104 (2017).
15. A. H. Dorrah, C. Rosales-Guzmán, A. Forbes, and M. Mojahedi, Phys. Rev. A **98**, 043846 (2018).
16. M. Corato-Zanarella, A. H. Dorrah, M. Zamboni-Rached, and M. Mojahedi, Phys. Rev. Appl. **9**, 024013 (2018).
17. P. Zhang, Y. Hu, D. Cannan, A. Salandrino, T. Li, R. Morandotti, X. Zhang, and Z. Chen, Opt. Lett. **37**, 2820 (2012).
18. P. Zhang, Y. Hu, T. Li, D. Cannan, X. Yin, R. Morandotti, Z. Chen, and X. Zhang, Phys. Rev. Lett. **109**, 193901 (2012).
19. Y. Aborahama, A. H. Dorrah, and M. Mojahedi, Opt. Express **28**, 24721 (2020).
20. J. Zhang, N. Pégard, J. Zhong, H. Adesnik, and L. Waller, Optica **4**, 1306 (2017).
21. G. Whyte and J. Courtial, New J. Phys. **7**, 117 (2005).
22. M. A. Seldowitz, J. P. Allebach, and D. W. Sweeney, Appl. Opt. **26**, 2788 (1987).
23. Y. Aborahama and M. Mojahedi, Phys. Rev. Appl. **15**, 044019 (2021).
24. Y. Aborahama, A. H. Dorrah, and M. Mojahedi, in *Conference on Lasers and Electro-Optics (CLEO)* (IEEE, 2020), pp. 1–2.

202.119.46.199 on 2021-10-27 11:12 UTC